

Investigating the electronic structure of high explosives with x-ray Raman spectroscopy

Oscar A. Paredes-Mellone¹, Michael H. Nielsen², John Vinson³, Konmeng Moua², K. Dean Skoien¹, Dimosthenis Sokaras^{1,*}, and Trevor M. Willey^{2,*}

¹SLAC National Accelerator Laboratory, 2575 Sand Hill Rd, Menlo Park, CA 94025 USA

²Lawrence Livermore National Laboratory, 7000 East Avenue, Livermore, CA 94551 USA

³Material Measurement Laboratory, National Institute of Standards and Technology, Gaithersburg, MD 20899 USA

*dsokaras@slac.stanford.edu, willey1@llnl.gov

ABSTRACT

We investigate the sensitivity and potential of a synergistic experiment-theory x-ray Raman spectroscopy (XRS) methodology on revealing and following the static and dynamic electronic structure of high explosive molecular materials. We show that advanced *ab-initio* theoretical calculations accounting for the core-hole effect based on the Bethe-Salpeter Equation (BSE) approximation are critical for accurately predicting the shape and the energy position of the spectral features of C and N core-level spectra. Moreover, the incident x-ray dose typical XRS experiments require can induce, in certain unstable structures, a prominent radiation damage at room temperature. Upon developing a compatible cryostat module for enabling cryogenic temperatures (≈ 10 K) we suppress the radiation damage and enable the acquisition of reliable experimental spectra in excellent agreement with the theory. Overall, we demonstrate the high sensitivity of the recently available state-of-the-art x-ray Raman spectroscopy capabilities in characterizing the electronic structure of high explosives. At the same time, the high accuracy of the theoretical approach may enable reliable identification of intermediate structures upon rapid chemical decomposition during detonation. Considering the increasing availability of x-ray free-electron lasers, such a combined experiment-theory approach paves the way for time-resolved dynamic studies of high explosives under detonation conditions.

Introduction

High explosive materials, used in a variety of civilian and military applications, release energy extremely rapidly when detonated. A challenge to a fundamental understanding of detonation phenomena is our inability to directly experimentally interrogate these rapid chemical kinetics within the bulk of these solid molecular materials. Particularly for dynamic detonation environments, theoretical and computational investigations have preceded experimental results by many years due to the complexity of experiments interrogating chemistry during detonation. As a prime example, the unique insensitivity to heat and shock and long reaction zone in tri-amino, tri-nitro benzene (TATB) may be correlated to the calculated rapid H₂O formation at the periphery of the TATB followed by formation of nitrogen heterocycles slowing detonation chemical reactions, but no experiments to date have verified this result¹. Similarly, theoretical and computational chemical kinetics and decomposition mechanisms during detonation have been performed on various materials such as hexanitrohexaazaisowurtzitane (CL-20)², 2,6-Diamino-3,5-dinitropyrazine-1-oxide (LLM-105)³, hexogen (RDX)⁴, octogen (HMX)⁵, and trinitrotoluene (TNT)⁶. Generally, the fundamental understanding of the underlying chemical kinetics may enable the targeted design of new explosives with desirable insensitivity and improved performance.

The element specificity of core-level spectroscopy can enable site-selective access to the local electronic structure providing information about neighboring atoms, coordination, and bonds. Application of core-level spectroscopies to high-explosives are scarce^{7,8}. The intrinsic limitations of soft x-ray techniques regarding sample preparation and environment, along with the requirement for bulk sensitivity to investigate chemical decomposition and evolution during detonation conditions, pose major limitations to absorption spectroscopies for such organic species. X-ray Raman scattering (XRS) spectroscopy⁹, a core-level photon-in/photon-out hard x-ray technique, emerges as a powerful tool to address these fundamental questions. XRS provides bulk sensitivity and allows access to absorption edges of low Z elements with hard x-rays avoiding in this way usual constraints inherent to UV/soft x-ray spectroscopies. A built-in limitation of XRS is the low inelastic scattering cross-section, which requires both high-brilliance x-ray sources and large solid angle multi-crystal spectrometers to perform experiments in reasonable acquisition times for suitable high-concentrated systems. These aspects have delayed and limited the application of XRS.

In this work, we establish a requisite static experimental and computational framework to characterize the electronic structure of common high explosives. Three materials investigated here represent both canonical and unique properties among

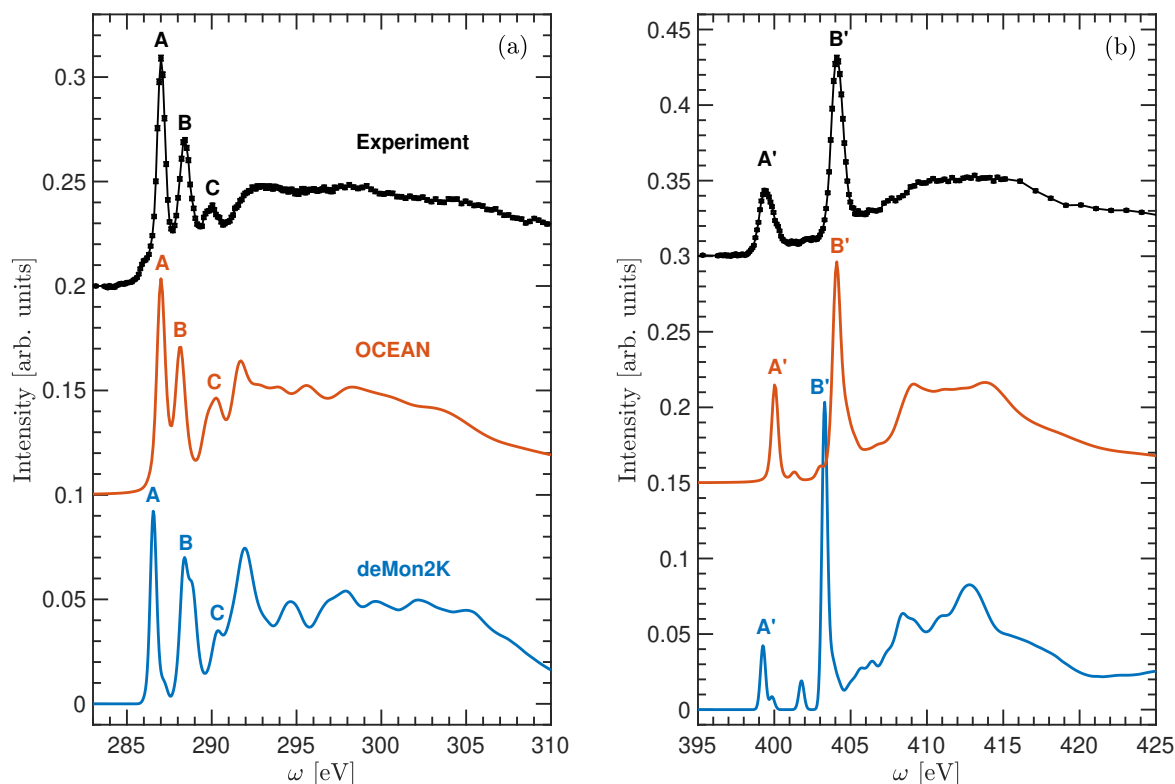


Figure 1. Experimental and theoretical 1s carbon (a) and nitrogen (b) X-ray Raman spectra of TATB.

explosives. TATB, an incredibly stable and insensitive high explosive, consists of alternating nitro (NO_2) and amino (NH_2) moieties attached to a central six-membered carbon ring, while hexanitrostilbene (HNS), also a relatively stable material, contains NO_2 but lacks NH_2 . These materials provide spectroscopic baselines for these two nitrogen groups that are often found in high explosives. CL-20, one of the most powerful manufactured explosives, is a cage structure, with saturated rather than aromatic carbon. By combining experimental and theoretical methods, we establish a synergistic framework to identify and distinguish un-detonated explosives from transient structures by unambiguously assigning spectral features to the molecular structure of the system. Ultimately, this systematic study of high-explosives upon static conditions sets the basis for future time-resolve dynamic experiments during detonation, by leveraging the increasing availability of x-ray free electron laser facilities around the globe¹⁰.

Results and discussions

Room temperature XRS measurements on TATB and HNS

The TATB carbon and nitrogen 1s XRS experimental spectra along with the corresponding OCEAN and deMon2K calculations are shown in Fig. 1. The main features in the experimental carbon 1s spectrum are: a small pre-edge shoulder with an onset at 285.8 eV, two strong sharp peaks at 287.02 eV (A) and 288.40 eV (B), and a lower intensity peak observed at 290.02 eV (C). Transition energies are listed in Table 1. Most of these features are well captured by the calculations both in terms of energy positions and intensities, with the exception of the low-energy pre-edge shoulder. Another difference between experiment and calculations is observed for energies above ≈ 291 eV, where both codes predict slightly more pronounced fine-structure than experimentally observed, something quite common for DFT approaches. Similarly, on the nitrogen 1s spectrum we observe two marked peaks at 399.40 eV (A') and 404.11 eV (B') as shown in Fig. 1 (b).

The excellent agreement between calculations and experiments, particularly for the BSE-based approach, allows us to associate the spectral resonances to the molecular and electronic structure of the system. The OCEAN code calculates the excited state (photoelectron—core-hole pair) wavefunction iteratively taking into account the core-hole interaction explicitly within the BSE approximation¹¹. Ultimately, this procedure provides the excited state 3D electron densities associated with the transitions. The excited state charge densities associated with the carbon and nitrogen spectral features are shown in

Table 1. Transition energies of noticeable spectral features. Listed energy values correspond to peak maximum with the exception of TATB pre-edge where the onset value is given instead¹². Note, only relative energies are calculated with OCEAN (see text), and peak A (B') of TATB was used to align the carbon (nitrogen) K edge.

Molecule	Feature	Energy transfer [eV]	OCEAN energy [eV]	deMon2K energy [eV]
TATB	pre-edge	285.78±0.07	-	-
	A	287.02±0.02	287.02 ^c	286.56
	B	288.40±0.02	288.14	288.40
	C	290.02±0.03	290.25	290.04
	A'	399.40±0.02	400.04	399.26
	B'	404.11±0.02	404.11 ^c	403.30
HNS	A	285.01±0.03	284.93	284.69
	B	285.88±0.02	285.59	285.80
	C	288.28±0.02	287.93	287.51
	A'	399.7±0.1	-	-
	B'	404.02±0.02	403.45	403.08
CL-20	A	287.84±0.04	-	-
		286.88±0.03 ^a	-	-
		286.91±0.03 ^b	-	-
	D	≈289 ^b	289.08	288.86
	B	291.61±0.08 ^a	-	-
	291.71±0.04 ^b	291.00	291.72	

^a 10 K - high dose.

^b 10 K - low dose.

^c OCEAN requires a single calibration energy

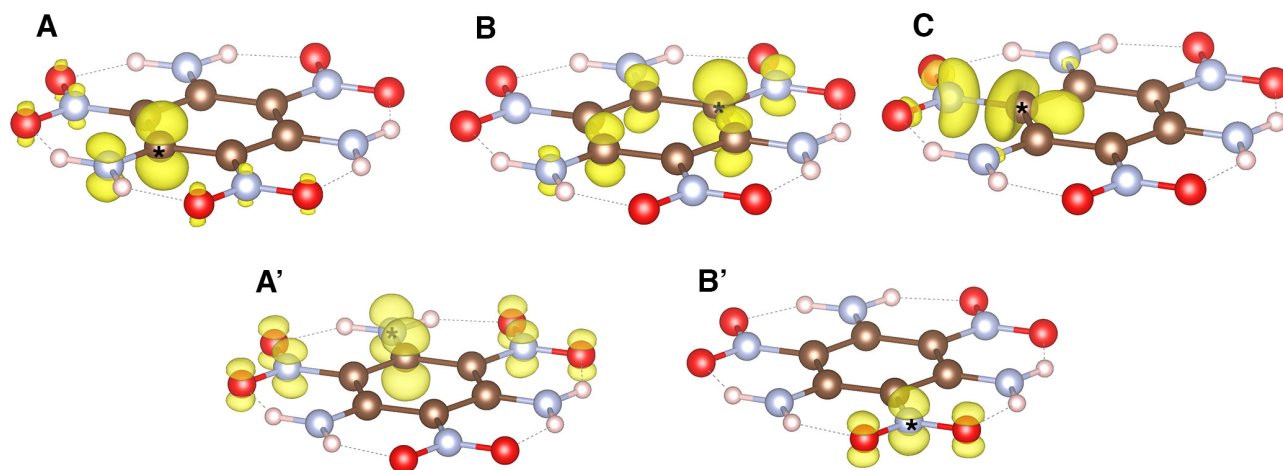


Figure 2. Excited state charge densities of carbon (top) and nitrogen (bottom) sites contributing to transitions as indicated in Fig. 1. Color code: Brown: carbon. Gray: nitrogen. Red: oxygen. White: hydrogen. Excited sites are indicated by an asterisk. Figures were made using VESTA.¹³

Fig. 2. These densities illustrate that the first (A) and second (B) peaks on the carbon $1s$ spectrum correspond to carbons bonded to NH_2 and NO_2 groups, respectively, and the probed states exhibit a strong p -like character. These results are in contrast with previous bond-assignments⁷ where, based on intramolecular charge transfer analysis, A and B were assigned to C- NO_2 and C- NH_2 moieties, respectively. The peak C observed at higher energies, has strong contribution from in-plane σ -like excitations from carbon sites bonded to NO_2 groups. The excited state electron densities associated to both peaks of the nitrogen $1s$ spectrum exhibit a dominant π -like character with nitrogen sites from NH_2 and NO_2 groups contributing to A' and B', respectively, though the former exhibits a higher degree of delocalization (see Fig. 2). Additional support to the energy positions found in this work for structures A (A') and B (B'), and the corresponding site assignments, is provided by previous x-ray photoelectron spectroscopy (XPS) results on N $1s$ core-level binding energies for different compounds bearing NH_x 399.5 ± 0.2 eV¹⁴, 400.4 ± 0.1 eV¹⁵, 400.49 ± 0.08 eV¹⁶ and NO_y 404.2 eV¹⁷, 403.9 eV¹⁷, 403.7 eV¹⁸, 403.6 eV¹⁹ groups.

Experimental and calculated carbon and nitrogen $1s$ spectra of HNS are shown in Figs. 3 (a) and (b), respectively. The first peak observed in the experimental carbon $1s$ spectrum has a sharp maximum (A) at 285.01 eV and a marked high-energy shoulder (B) at 285.88 eV, followed by another sharp structure (C) at 288.28 eV. For the nitrogen edge, an intense sharp peak (B') at 404.02 eV appears and a very weak pre-edge structure (A') at 399.7 eV. The pristine HNS molecule constitutes of a single nitrogen species formed by six NO_2 groups. Therefore, the weak pre-edge structure represents a minimal contribution of contamination and/or early radiation damage. Besides this, the main observed features are nicely reproduced by both calculation approaches, although OCEAN predicts energy positions and intensities of the spectral features in a noticeably better agreement with the experiment. Electron charge densities associated with the relevant structures in the spectra are shown in Fig. 4. The first transitions contributing to peak A arise from p -like symmetry charge densities highly localized around the excited carbon sites. Those transitions come from C-H moieties and the carbons bridging between the two C6 rings. The major contribution in transitions at B comes from more delocalized states associated with carbons in the C- NO_2 groups exhibiting a π -like bonding between the CN sites. At feature C, higher energy transitions from C- NO_2 carbon moieties contribute to largely delocalized charge densities. All nitrogens contributing to B' exhibit similar p -like symmetry charge densities localized around the atoms within the NO_2 groups.

Room vs cryogenic temperature XRS measurements on CL-20

Carbon $1s$ spectra of CL-20 are shown in Fig. 5. The first set of measurements was performed at room temperature, same as for TATB and HNS with an acquisition time per individual spectrum of ≈ 260 s²⁰. The bottom spectrum in Fig. 5a shows an intense sharp peak at 287.84 eV (A), followed by a marked feature at 289.6 eV and two prominent broad structures (B and C) at higher energies. The corresponding calculated OCEAN and deMon2K spectra are shown in 5 (b). The spectral features calculated by both codes are very consistent, predicting similar intensities, peak energy positions and overall spectral shapes. When compared to the measured RT CL-20 spectra striking differences are evident suggesting quick radiation damage from the intense incident x-ray beam. Radiation damage on high-explosives has been previously reported on x-ray diffraction experiments using synchrotron radiation²¹. Within the biochemistry and biology communities it is well known that such effects

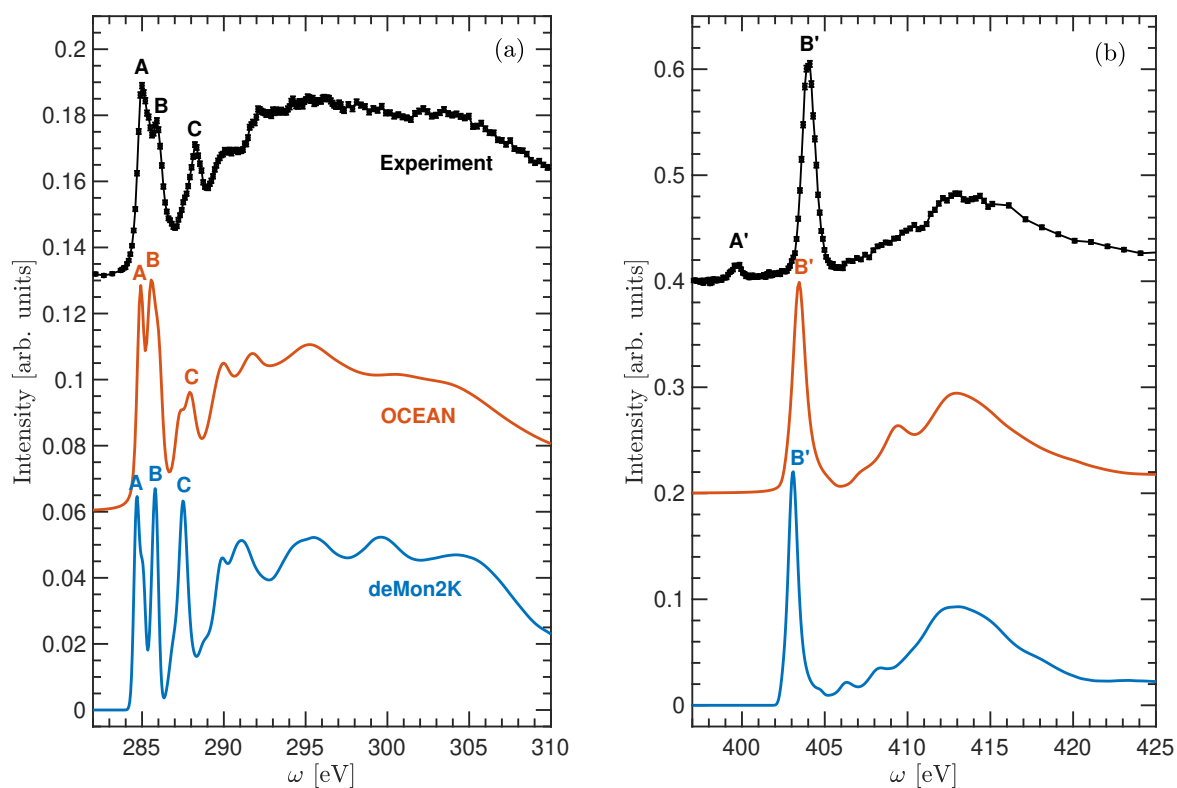


Figure 3. Experimental and theoretical 1s carbon (a) and nitrogen (b) X-ray Raman spectra of HNS.

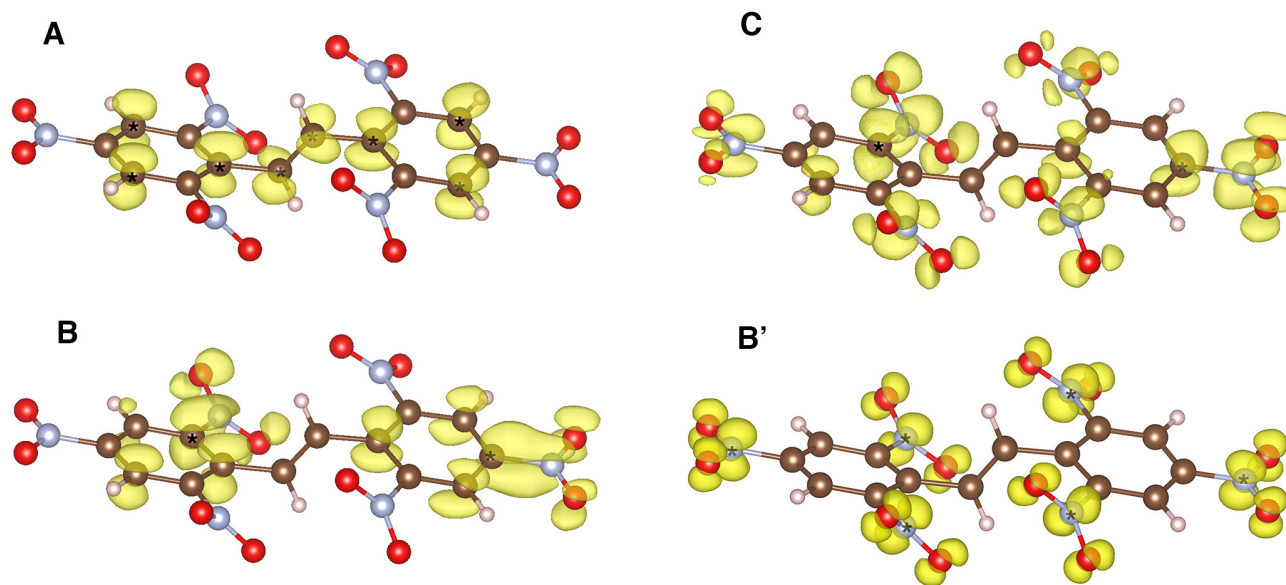


Figure 4. Excited state charge densities contributing to peaks in the carbon and nitrogen 1s spectra as indicated in Fig. 3. Atoms color code and labeling as in Fig. 2.

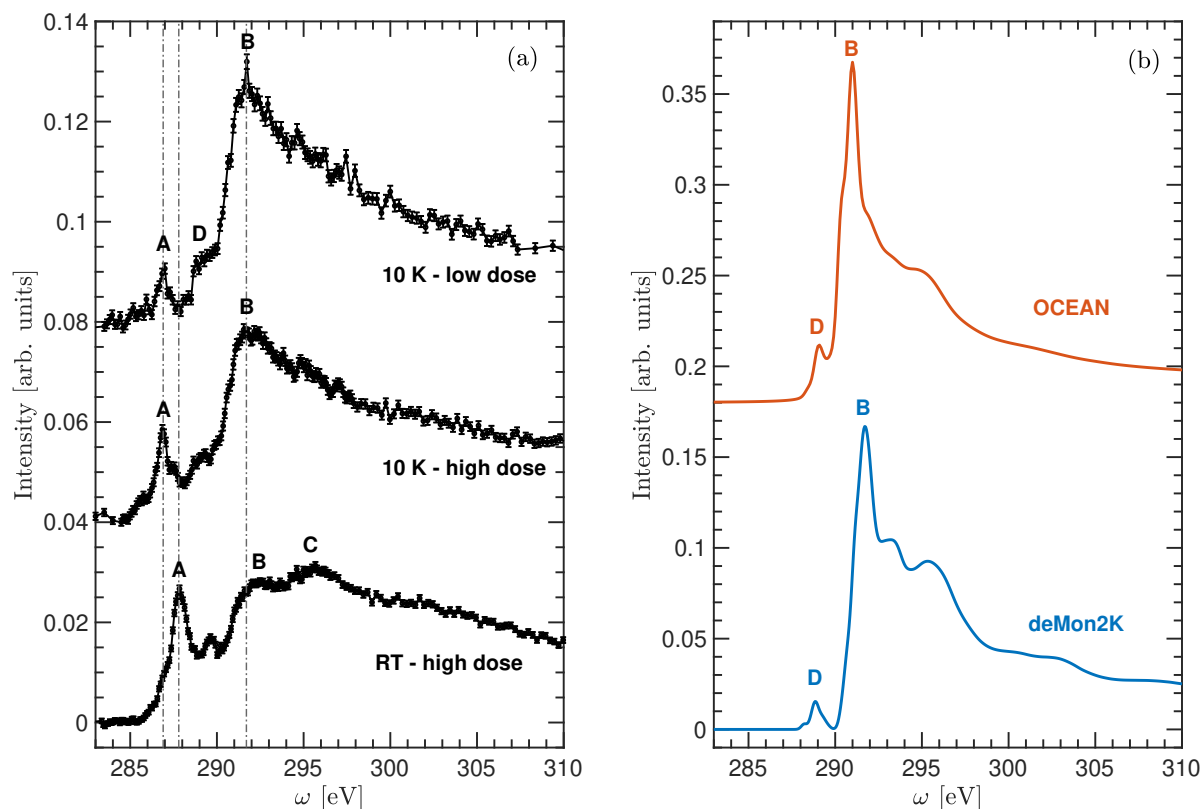


Figure 5. Experimental (a) and theoretical (b) $1s$ carbon x-ray Raman spectra of CL-20. Experimental spectra were taken for different radiation dose and temperature as indicated.

get suppressed when samples are kept at cryogenic temperatures^{22,23}, therefore measuring radiation-sensitive high-explosive molecules under cryogenic conditions could allow the acquisition of reliable experimental spectra for the pristine molecular structures. Here, we designed a custom cryostat compatible with the geometry of the XRS experiments which adopted and enabled x-ray Raman experiments at cryogenic temperatures down to ≈ 10 K. In this way, measuring CL-20 at 10K, and for similar radiation dose as in room temperature measurements (≈ 210 s per spectrum), major spectral changes are observed in the carbon $1s$ spectrum. The first peak A shifts to lower energies and its intensity decreases. Additionally, the broad structure at higher energies becomes more intense and pronounced at 291.61 eV (B). After further reducing the radiation dose down to ≈ 55 s per spectrum, a similar trend is observed, the intensity at A diminishes even further with no apparent shift in energy and B evolves into a marked peak. Additionally, a pre-edge shoulder emerges around ≈ 289 eV (D) which corresponds very well with theoretical spectra. The observed systematic changes in the spectral features with increasing radiation dose and temperature, along with the remarkable agreement between simulated and low-dose spectra measured at 10 K, are conclusive evidence that the appearance of peak A and the decrease in intensity at B are spectral fingerprints associated with radiation damage and do not represent features of the pristine molecular structure.

Theoretically, unimolecular decomposition pathways in high-explosives have been investigated by means of density functional theory^{2,24} and *ab initio* molecular dynamics under high-temperature conditions^{25–27}. By assessing the high-sensitivity of x-ray Raman spectroscopy to the local electronic and molecular structures of high-explosives, and our recently developed capabilities for investigating radiation sensitive systems, this study set the basis for future systematic XRS experiments to investigate such decomposition mechanisms and shed light on the fundamental chemistry processes high-explosives undergo during initial decomposition steps. Performing high- q x-ray Raman experiments could also provide complementary/additional information for characterizing the electronic and molecular structure of these materials through the opening of strong contributions to the XRS spectra of non-dipole-like excitation channels.

Conclusion

We have investigated high-explosives with x-ray Raman scattering spectroscopy. By combining experimental and advanced theoretical methods, excellent agreement between measurements and simulations is achieved. The BSE approximation has proven to be fundamental in accurately describing near-edge spectral features, relative intensities, and energy positions. For the case of TATB and HNS, the experiment-theory agreement allowed an unambiguous assignment of spectral features to specific moieties of the system. For systems with high sensitivity to radiation damage, we developed capabilities to perform x-ray Raman scattering experiments at cryogenic temperatures, which proved to suppress the damage induced by the intense incident x-ray beam. XRS measurements at cryogenic temperatures allowed reliable data acquisition of the pristine, undamaged system. These results constitute conclusive evidence of the suitability and sensitivity of XRS spectroscopy in identifying spectral fingerprints in high-explosives.

Methods

Sample preparation and handling

Samples were prepared by uniaxially pressing materials into small disks to minimize the energetic material in any given sample. For TATB and HNS these disks were 3 mm in diameter and had a weight of 10 mg. The CL-20 samples were pressed into 6 mm diameter, 40 mg disks to accommodate mounting within the cryostat, and to enable multiple fresh acquisition positions on a given sample. The room temperature samples were mounted using SEM adhesive tape. Cryostat samples were mounted in a custom-fabricated cassette to hold the samples in place without imposing any mechanical stress. All explosive samples were transported and handled under U.S. Department of Transportation (DOT) and Department of Energy (DOE) regulations.

Experiment

The x-ray Raman scattering (XRS) spectroscopy experiments were performed at BL 15-2 at Stanford Synchrotron Radiation Lightsource (SSRL). The undulator radiation was monochromated using a liquid nitrogen cooled Si(311) double-crystal monochromator. Two Kirkpatrick–Baez (KB) mirrors focused the x-ray beam to a $50 \mu\text{m} \times 150 \mu\text{m}$ (H \times V) size at the sample position with a photon flux of 3×10^{12} photons/s to 4×10^{12} photons/s. All samples were measured in reflection geometry (along the horizontal plane) using a grazing angle of $\approx 2^\circ$ to 3° in order to optimize counting statistics and minimize incident beam areal power density. The XRS spectrometer at the BL 15-2 end-station constitutes of 40 diced Si(110) analyzer crystals and more details are given elsewhere²⁸. The center of the spectrometer corresponds to a forward scattering angle of $\approx 40^\circ$ with an angular opening of about 50° . Measurements of the energy-loss spectra were performed in the so-called inverse geometry, *i.e.* the analyzed energy was kept fixed at $\omega_2 \approx 6.46$ keV while varying the incident beam energy ω_1 . Hence, the XRS spectra are measured by scanning the energy transfer $\omega = \omega_1 - \omega_2$ around each absorption edge. The total energy resolution at the operated Si(440) diffraction order and for the adopted grazing geometry and beam size was measured to be ≈ 0.33 eV via the full width at half maximum (FWHM) of the elastic peak. The angular range of the spectrometer captures momentum transfers between $0.7 \text{ a.u.} \leq q \leq 2.9 \text{ a.u.}$ For these q values and for the studied absorption edges C and N, the dipole approximation $qa < 1$ (a being the $1s$ core electron orbital radius) is fulfilled. Hence, the information accessible by XRS within this regime is equivalent to that of x-ray absorption spectroscopy. For each sample and absorption edge, several individual x-ray Raman spectra were collected across numerous fresh sample spots under the same experimental conditions. The measured intensity of each spectrum was normalized to the monitored intensity and used for extracting an averaged spectrum. Accurate energy-loss calibration was obtained by periodically measuring the elastic line. The variance in the elastic line energy position, as obtained by fitting a Gaussian profile, was ≤ 0.01 eV. To extract the core-electron contribution from the whole energy-loss spectrum, we performed a combined fitting procedure scheme similar to the one described elsewhere^{29,30}. An exponential decay function was fitted for energy transfers below the $1s$ electron excitation onset to account for the high energy tail of the valence electron spectrum. Simultaneously, we approximate the high-energy tail of the whole energy-loss spectrum by the exponential decay function plus the atomic background as calculated with the FEFF code³¹. The latter was used to approximate the high-energy tail of the core-electron contribution. Finally, the fitted exponential function obtained out of this combined procedure was subtracted from the spectra to obtain the core electron contribution. Additional details are provided in the supplementary material.

Calculations

Geometry optimizations and numerical frequency calculations were performed using the B3LYP exchange-correlation functional with triple-zeta basis functions with the ORCA 4.2.1 package³². For the optimized geometries, vibrational frequencies were calculated and no imaginary frequencies were obtained from the analysis. The theoretical x-ray spectra were calculated with two different approaches. First, a density functional theory (DFT) based formalism using Gaussian type orbitals as basis sets and the so-called transition potential approximation for determining the oscillator strengths was used as implemented in

the deMon2K package³³. Second, a plane-wave DFT formalism which takes into account excitonic effects explicitly within the Bethe-Salpeter equation (BSE) approach was used as implemented in the OCEAN code^{34,35}. Unlike deMon2K which calculates only x-ray absorption spectra, the OCEAN code can calculate x-ray Raman spectra by accounting for the finite momentum transfer, which can enable the interpretation of high- q XRS experiments. Details of the x-ray spectra calculations are given in the supplementary material. The theoretical spectra were broadened with an energy-dependent Lorentzian and constant Gaussian line shapes as done elsewhere^{36,37}. The former accounts for core-hole lifetime and the latter for instrumental resolution. For the TATB carbon (nitrogen) edge, we applied a Lorentzian broadening of 0.1 eV for $\omega < 286$ eV ($\omega < 403$ eV), which then linearly increased up to 3 eV between $286 \text{ eV} \leq \omega \leq 310$ eV ($403 \text{ eV} \leq \omega \leq 420$ eV). Then, the spectra were broadened with a Gaussian lineshape of FWHM=0.33 eV. A similar broadening was applied for plotting the HNS and CL-20 theoretical spectra.

References

1. Manaa, M. R., Reed, E. J., Fried, L. E. & Goldman, N. Nitrogen-rich heterocycles as reactivity retardants in shocked insensitive explosives. *J. Am. Chem. Soc.* **131**, 5483–5487, DOI: [10.1021/ja808196e](https://doi.org/10.1021/ja808196e) (2009). PMID: 19323461, <https://doi.org/10.1021/ja808196e>.
2. Okovytyy, S., Kholod, Y., Qasim, M., Fredrickson, H. & Leszczynski, J. The mechanism of unimolecular decomposition of 2,4,6,8,10,12-hexanitro-2,4,6,8,10,12-hexaazaisowurtzitane. a computational dft study. *The J. Phys. Chem. A* **109**, 2964–2970, DOI: [10.1021/jp045292v](https://doi.org/10.1021/jp045292v) (2005). PMID: 16833616, <https://doi.org/10.1021/jp045292v>.
3. Hamilton, B. W. *et al.* Predicted reaction mechanisms, product speciation, kinetics, and detonation properties of the insensitive explosive 2,6-diamino-3,5-dinitropyrazine-1-oxide (llm-105). *The J. Phys. Chem. A* **125**, 1766–1777, DOI: [10.1021/acs.jpca.0c10946](https://doi.org/10.1021/acs.jpca.0c10946) (2021). PMID: 33617263, <https://doi.org/10.1021/acs.jpca.0c10946>.
4. Nomura, K.-i. *et al.* Dynamic transition in the structure of an energetic crystal during chemical reactions at shock front prior to detonation. *Phys. Rev. Lett.* **99**, 148303, DOI: [10.1103/PhysRevLett.99.148303](https://doi.org/10.1103/PhysRevLett.99.148303) (2007).
5. Zhou, T.-T. & Huang, F.-L. Effects of defects on thermal decomposition of hmx via reaxff molecular dynamics simulations. *The J. Phys. Chem. B* **115**, 278–287, DOI: [10.1021/jp105805w](https://doi.org/10.1021/jp105805w) (2011). PMID: 21142162, <https://doi.org/10.1021/jp105805w>.
6. Liu, H. *et al.* Reaxff molecular dynamics simulations of shock induced reaction initiation in tnt. *AIP Adv.* **9**, 015202, DOI: [10.1063/1.5047920](https://doi.org/10.1063/1.5047920) (2019). <https://doi.org/10.1063/1.5047920>.
7. Kakar, S. *et al.* Electronic structure of the energetic material 1,3,5-triamino-2,4,6-trinitrobenzene. *Phys. Rev. B* **62**, 15666–15672, DOI: [10.1103/PhysRevB.62.15666](https://doi.org/10.1103/PhysRevB.62.15666) (2000).
8. Vila, F. D., Jach, T., Elam, W. T., Rehr, J. J. & Denlinger, J. D. X-ray emission spectroscopy of nitrogen-rich compounds. *The J. Phys. Chem. A* **115**, 3243–3250, DOI: [10.1021/jp108539v](https://doi.org/10.1021/jp108539v) (2011). PMID: 21452848, <https://doi.org/10.1021/jp108539v>.
9. Schülke, W. *Electron dynamics by inelastic X-ray scattering* (Oxford University Press, 2007).
10. Willey, T. New frontiers in experimentally observing detonation properties. *Propellants, Explos. Pyrotech.* **44**, 259–261, DOI: <https://doi.org/10.1002/prop.201980331> (2019). <https://onlinelibrary.wiley.com/doi/pdf/10.1002/prop.201980331>.
11. Vinson, J., Jach, T., Müller, M., Unterumsberger, R. & Beckhoff, B. Quasiparticle lifetime broadening in resonant x-ray scattering of nh_4no_3 . *Phys. Rev. B* **94**, 035163, DOI: [10.1103/PhysRevB.94.035163](https://doi.org/10.1103/PhysRevB.94.035163) (2016).
12. Uncertainties were determined by error propagation on the zero-crossing of the experimental data first (second) derivative for the peak maximum (onset).
13. Momma, K. & Izumi, F. VESTA3 for three-dimensional visualization of crystal, volumetric and morphology data. *J. Appl. Crystallogr.* **44**, 1272–1276, DOI: [10.1107/S0021889811038970](https://doi.org/10.1107/S0021889811038970) (2011).
14. Gonella, G. *et al.* Ultrahigh vacuum deposition of l-cysteine on Au(110) studied by high-resolution x-ray photoemission: From early stages of adsorption to molecular organization. *The J. Phys. Chem. B* **109**, 18003–18009, DOI: [10.1021/jp051549t](https://doi.org/10.1021/jp051549t) (2005). PMID: 16853311, <https://doi.org/10.1021/jp051549t>.
15. Rudysh, M. Y. *et al.* Ionicity and birefringence of α - LiNH_4SO_4 crystals: ab initio dft study, x-ray spectroscopy measurements. *RSC Adv.* **7**, 6889–6901, DOI: [10.1039/C6RA27386F](https://doi.org/10.1039/C6RA27386F) (2017).
16. Rudysh, M. *et al.* Ab initio calculations of the electronic structure and specific optical features of β - LiNH_4SO_4 single crystals. *Phys. B: Condens. Matter* **528**, 37–46, DOI: <https://doi.org/10.1016/j.physb.2017.10.085> (2018).
17. Aduru, S., Contarini, S. & Rabalais, J. W. Electron-, x-ray-, and ion-stimulated decomposition of nitrate salts. *The J. Phys. Chem.* **90**, 1683–1688, DOI: [10.1021/j100399a045](https://doi.org/10.1021/j100399a045) (1986). <https://doi.org/10.1021/j100399a045>.

18. Bandis, C., Scudiero, L., Langford, S. & Dickinson, J. Photoelectron emission studies of cleaved and excimer laser irradiated single-crystal surfaces of NaNO_3 and NaNO_2 . *Surf. Sci.* **442**, 413–419, DOI: [https://doi.org/10.1016/S0039-6028\(99\)00953-X](https://doi.org/10.1016/S0039-6028(99)00953-X) (1999).
19. Baltrusaitis, J., Jayaweera, P. M. & Grassian, V. H. XPS study of nitrogen dioxide adsorption on metal oxide particle surfaces under different environmental conditions. *Phys. Chem. Chem. Phys.* **11**, 8295–8305, DOI: [10.1039/B907584D](https://doi.org/10.1039/B907584D) (2009).
20. Acquisition times listed in text correspond to individual spectrum. Spectra showed in plots are constructed by averaging over several individual spectra as indicated in text.
21. Giefers, H., Pravica, M., Yang, W. & Liermann, P. Radiation-induced decomposition of explosives under extreme conditions. *J. Phys. Chem. Solids* **69**, 2208–2212, DOI: <https://doi.org/10.1016/j.jpccs.2008.03.034> (2008). Study of Matter Under Extreme Conditions 2007.
22. Meents, A., Gutmann, S., Wagner, A. & Schulze-Briese, C. Origin and temperature dependence of radiation damage in biological samples at cryogenic temperatures. *Proc. Natl. Acad. Sci.* **107**, 1094–1099, DOI: [10.1073/pnas.0905481107](https://doi.org/10.1073/pnas.0905481107) (2010). <https://www.pnas.org/doi/pdf/10.1073/pnas.0905481107>.
23. de la Mora, E. *et al.* Radiation damage and dose limits in serial synchrotron crystallography at cryo- and room temperatures. *Proc. Natl. Acad. Sci.* **117**, 4142–4151, DOI: [10.1073/pnas.1821522117](https://doi.org/10.1073/pnas.1821522117) (2020). <https://www.pnas.org/doi/pdf/10.1073/pnas.1821522117>.
24. Kumar, M. A., Ashutosh, P. & Vargeese, A. A. Decomposition mechanism of hexanitrohexaazaisowurtzitane (cl-20) by coupled computational and experimental study. *The J. Phys. Chem. A* **123**, 4014–4020, DOI: [10.1021/acs.jpca.9b01197](https://doi.org/10.1021/acs.jpca.9b01197) (2019). PMID: 30995040, <https://doi.org/10.1021/acs.jpca.9b01197>.
25. Isayev, O., Gorb, L., Qasim, M. & Leszczynski, J. Ab initio molecular dynamics study on the initial chemical events in nitramines: Thermal decomposition of cl-20. *The J. Phys. Chem. B* **112**, 11005–11013, DOI: [10.1021/jp804765m](https://doi.org/10.1021/jp804765m) (2008). PMID: 18686996, <https://doi.org/10.1021/jp804765m>.
26. Wang, F. *et al.* Thermal decomposition mechanism of cl-20 at different temperatures by reaxff reactive molecular dynamics simulations. *The J. Phys. Chem. A* **122**, 3971–3979, DOI: [10.1021/acs.jpca.8b01256](https://doi.org/10.1021/acs.jpca.8b01256) (2018). PMID: 29620895, <https://doi.org/10.1021/acs.jpca.8b01256>.
27. Chen, L. *et al.* Thermal decomposition mechanism of 2,2,4,4,6,6-hexanitrostilbene by reaxff reactive molecular dynamics simulations. *The J. Phys. Chem. C* **122**, 19309–19318, DOI: [10.1021/acs.jpcc.8b03463](https://doi.org/10.1021/acs.jpcc.8b03463) (2018). <https://doi.org/10.1021/acs.jpcc.8b03463>.
28. Sokaras, D. *et al.* A high resolution and large solid angle x-ray raman spectroscopy end-station at the stanford synchrotron radiation lightsource. *Rev. Sci. Instruments* **83**, 043112, DOI: [10.1063/1.4704458](https://doi.org/10.1063/1.4704458) (2012). <https://doi.org/10.1063/1.4704458>.
29. Sternemann, H. *et al.* An extraction algorithm for core-level excitations in non-resonant inelastic X-ray scattering spectra. *J. Synchrotron Radiat.* **15**, 162–169, DOI: [10.1107/S0909049508001696](https://doi.org/10.1107/S0909049508001696) (2008).
30. Huotari, S. *et al.* X-ray-Raman-scattering-based EXAFS beyond the dipole limit. *J. Synchrotron Radiat.* **19**, 106–113, DOI: [10.1107/S0909049511039422](https://doi.org/10.1107/S0909049511039422) (2012).
31. Rehr, J. J., Kas, J. J., Vila, F. D., Prange, M. P. & Jorissen, K. Parameter-free calculations of x-ray spectra with feff9. *Phys. Chem. Chem. Phys.* **12**, 5503–5513, DOI: [10.1039/B926434E](https://doi.org/10.1039/B926434E) (2010).
32. Neese, F., Wennmohs, F., Becker, U. & Riplinger, C. The orca quantum chemistry program package. *The J. Chem. Phys.* **152**, 224108, DOI: [10.1063/5.0004608](https://doi.org/10.1063/5.0004608) (2020). <https://doi.org/10.1063/5.0004608>.
33. Salahub, D. R. *et al.* QM/MM calculations with deMon2k. *Molecules* **20**, 4780–4812, DOI: [10.3390/molecules20034780](https://doi.org/10.3390/molecules20034780) (2015).
34. Gilmore, K. *et al.* Efficient implementation of core-excitation bethe–salpeter equation calculations. *Comput. Phys. Commun.* **197**, 109–117, DOI: <https://doi.org/10.1016/j.cpc.2015.08.014> (2015).
35. Vinson, J., Rehr, J. J., Kas, J. J. & Shirley, E. L. Bethe-salpeter equation calculations of core excitation spectra. *Phys. Rev. B* **83**, 115106, DOI: [10.1103/PhysRevB.83.115106](https://doi.org/10.1103/PhysRevB.83.115106) (2011).
36. Sakko, A., Hakala, M., Soinenen, J. A. & Hämäläinen, K. Density functional study of x-ray raman scattering from aromatic hydrocarbons and polyfluorene. *Phys. Rev. B* **76**, 205115, DOI: [10.1103/PhysRevB.76.205115](https://doi.org/10.1103/PhysRevB.76.205115) (2007).
37. Sakko, A. *et al.* Inelastic x-ray scattering and vibrational effects at the k-edges of gaseous n_2 , n_2o , and co_2 . *Phys. Chem. Chem. Phys.* **13**, 11678–11685, DOI: [10.1039/C1CP20295B](https://doi.org/10.1039/C1CP20295B) (2011).

Acknowledgements

This work was performed under the auspices of the U.S. Department of Energy by Lawrence Livermore National Laboratory under Contract DE-AC52-07NA27344. Use of the Stanford Synchrotron Radiation Lightsource, SLAC National Accelerator Laboratory, was supported by the U.S. Department of Energy, Office of Science, Office of Basic Energy Sciences under Contract No. DE-AC02-76SF00515. This research used resources of the National Energy Research Scientific Computing Center (NERSC), a U.S. Department of Energy Office of Science User Facility operated under Contract No. DE-AC02-05CH11231. Some of the computing for this project was performed on the Sherlock cluster at Stanford University. We would like to thank Stanford University and the Stanford Research Computing Center for providing computational resources and support that contributed to these research results. We acknowledge Alex Baker, Jerry Cundiff, Kenneth Hansen, Franco Gagliardi, and High Explosives Applications Facility (HEAF) staff at LLNL in preparation for, and execution of, these experiments. Certain commercial equipment, instruments, or materials are identified in this paper in order to specify the experimental procedure adequately. Such identification is not intended to imply recommendation or endorsement by NIST, nor is it intended to imply that the materials or equipment identified are necessarily the best available for the purpose. LLNL-JRNL-840241.

Author Contributions statement

O.A.P.M., D.S., T.M.W. designed and performed the experiments. K.M. prepared and handled high-explosive samples. K.D.S. modified the cryostat for XRS experiments. O.A.P.M. analyzed the experimental data. O.A.P.M., D.S., T.M.W., and M.H.N. interpreted the experimental data. O.A.P.M. and J.V. performed the *ab initio* calculations. O.A.P.M., D.S., and T.M.W. wrote the manuscript with contributions from all authors.

Competing interests

There are no conflicts of interest to declare.

Data availability

The datasets used and/or analysed during the current study available from the corresponding author on reasonable request